Effects of ball milling on the electrochemical capacity and interfacial stability of Li_2MnO_3 cathode materials

Jianan Xu,[¶Φ] *Lori Kaufman,* [†Φ] *Francisco C. Robles Hernández,*[‡] *Atin Pramanik,*[¶*] *Ganguli Babu,* [¶] *Nanda Jagjit,*[§] *Bryan D. McCloskey,*[†,‖,*] *Pulickel M. Ajayan*[¶,*]

[¶]Department of Materials Science and NanoEngineering, Rice University, Houston, Texas 77005, United States

[†]Department of Chemical & Biomolecular Engineering, University of California, Berkeley, Berkeley, California 94720, United States

[‖]Energy Storage & Distributed Resources Division, Lawrence Berkeley National Laboratory, Berkeley, California 94720, United States

‡Mechanical Engineering Technology, University of Houston, Houston, Texas 77204, United States

[§]Chemical Sciences Division, Oak Ridge National Laboratory, Oak Ridge, Tennessee 37831, United States

*atinpramanik1990@gmail.com; bmcclosk@berkeley.edu; ajayan@rice.edu

Φ These authors contributed equally to this work.

ABSTRACT: The cycling mechanism of Li_2MnO_3 cathode materials synthesized by conventional solid-state methods at high temperatures (800-900 °C) has been intensively investigated. Previous studies showed that CO_2 and O_2 gas evolution

accounts for a majority of the charge capacity, followed by some Mn reduction during the discharge process. In this work, we analyze the effects of ball milling on the structure, surface contaminant and electrochemical capacity of Li_2MnO_3 cathode material, with or without a graphitic fluoride (C-F) additive, while C-F is added with the intention to form a protective coating layer that reduces unwanted reactions with the electrolyte during later electrochemical cycling. We find that the C-F ball-milled material shows $Li_2MnO_3/LiMnO_2$ composite phases, while the purely ball-milled material shows a single Li_2MnO_3 phase. Furthermore, we characterize surface species and gas evolution during the first cycle, which reveals the decomposition of Li_2CO_3 and the carbonate electrolyte during the first charge, especially during the high potential region (> 4.4 V), and the electrochemical reduction of only a small fraction of the evolved gas on the first discharge (< 2.75 V). The repetitive nature of this process is further demonstrated by the appearance during charge and disappearance during discharge of Mn $2p_{3/2}$ X-ray photoelectron spectroscopy (XPS) spectra's signal during the first two cycles. These processes result in a first discharge specific capacity of only 155 mAh/g and 170 mAh/g, after a first charge specific capacity of 210 mAh/g and 320 mAh/g for the purely ball milled and ball milled with C-F materials, respectively. These studies demonstrate the interfacial instability introduced by ball milling, though the electrochemical capacity is significantly increased, necessitating further investigation to determine whether ball milling can be used to activate Mn-containing cathode materials.

1. Introduction

Lithium-ion batteries are a leading modern technology that benefits from an optimal energy density and power density combination. The cathode, one of the main components in a battery system, plays an essential role in determining the price and energy density. A typical commercial high energy density cathode is $LiNi_xMn_yCo_zO_2$ where x+y+z =1 (NMC) or $LiNi_uCo_vAl_wO_2$ where u+v+w=1 (NCA).[1-2] However, due to the scarcity of transition metals Ni and Co, there is always a strong economic motivation for developing economical Ni- and Co-free cathode materials. Therefore, $LiMnO_2$ and $LiMn_2O_4$ cathode materials have been shown significant attention during the past several decades.[3-4] Recently, the motivation has been shifted to exploit the charging or cycling mechanism of Li_2MnO_3, which was originally considered electrochemically inactive but was later found to deliver >300 mAh/g on the first charge up to 4.8 V vs Li^+/Li.[5-8] Using differential electrochemical mass spectrometry (DEMS) as a powerful tool to monitor the quantity of each species of gas generated during electrochemical cycling, Rana et al. have reported that the first charge capacity is predominantly derived first from the decomposition of surface Li_2CO_3 into CO_2 at the low potential stage of <4.6 V, followed by O_2 release from lattice oxygen oxidation in the high potential region.[6] On the other hand, Zhuo et al. studied the bulk composition of Li_2MnO_3 during cycling, where they combined high-efficiency mapping of resonant inelastic X-ray scattering (mRIXS) and X-ray absorption spectroscopy (XAS).[8] They argue that $Mn^{3+/4+}$ accounts for the bulk redox reaction starting from the first discharge process, where the initial charge plateau is from Li_2CO_3 decomposition and lattice oxygen release, with no reversible lattice oxygen redox reaction.

Besides traditional layered cathode materials, cation-disordered rock salt (DRX) materials have also been extensively explored with various stoichiometries, such as Li-Ni-Ti/Nb-O-F and Li-Mn-Ti/Nb-O-F.[9-11] The general synthesis temperature usually reaches 950-1000 ℃ for Mn-based DRX materials, which results in a particle morphology where the particles exceed 5 μm in size.[12] Kan et al. also reported synthesizing 6 μm size single crystal $Li_{1.3}Mn_{0.4}Nb_{0.3}O_2$ using a molten salt method.[13] Nevertheless, ball mill treatment is inevitably employed to break down the large particles to realize the gravimetric specific capacity closer to the theoretical calculation.[13-15] Though ball milling is primarily used to solve the sluggish kinetics of Li^+ diffusion in DRX materials, it is adopted to synthesize a new cation disordered phase of Li_2MnO_3 through a 86hrs long process. While this work reports a good electrochemical activity as 320 mAh/g first discharge specific capacity, the potential effects on the interfacial chemistry and stability of the Li_2MnO_3 cathode material is not addressed.[16]

In this work, we first synthesize Li_2MnO_3 using a conventional solid-state reaction at 800 ℃, followed by ball milling treatment.[17] Graphitic fluoride is also introduced as an additive during the ball milling process, which may have different effects on the surface chemistry compared to a purely ball milled sample. Combining X-ray diffraction (XRD), transmission electron microscopy (TEM), X-ray photoelectron microscopy (XPS), and acid titration, we monitor the phase changes of the ball milled Li_2MnO_3 as well as the amount of surface contaminant Li_2CO_3. We also employ DEMS to monitor the outgassing during electrochemical cycling and the pressure of a closed-

cell system is recorded by a pressure gauge. Through the above characterization techniques, the enhanced electrochemical capacity of the ball milled materials is reasonably assigned to Li_2CO_3 decomposition, electrolyte decomposition and possible $Mn^{3+/4+}$ redox reaction. Our results provide a perspective to consider that ball milling, which is used to access more of the electrochemical capacity, will induce stimulating surface effects on the cathode materials.

2. Experimental Methods

Materials synthesis and characterizations

Pristine Li_2MnO_3 was synthesized from Li_2CO_3 and MnO_2 (all from Sigma-Aldrich). The two precursors were stoichiometrically weighed, hand-mixed by mortar and pestle, then transferred to an alumina crucible and calcined at 800 °C for 10 hours in a muffle furnace under an air atmosphere. For the ball milling process, 1.0 g pristine Li_2MnO_3 was added into the milling jar with ZrO_2 as milling media, with a 1:15 material to ball mass ratio. In the case of the BMC-F material, 100 mg graphitic fluoride [$(CF_x)_n$, x~1.1, Sigma-Aldrich] was used as an additive in the ball milling procedure. The SPEX 8000 mill equipment was used to ball mill each material for 4.5 hours (1060 cycles/minute).

After ball milling, the materials were collected under ambient conditions, (the cathode electrode was prepared under the air atmosphere) and stored in a glovebox for further characterization. An FEI Quanta 400 scanning electron microscope was used to observe the morphology of pristine Li_2MnO_3, BMP and BMC-F samples. Powder X-ray diffraction (PXRD) data were recorded using a Rigaku Smartlab II with Cu-Kα

radiation (λ = 1.54 Å) to obtain phase purity crystallographic information of the materials. The TEM observations were carried out in a JEOL 2100 operated at 200 kV. Images in bright field and High-Resolution Transmission Electron Microscopy (HRTEM) were collected. The analysis was done using CIF files from Li_2MnO_3 (ICDD 04-011-3411) and $LiMnO_2$ (ICDD 04-019-9854) and the software Vesta®. Mn $2p_{3/2}$ spectra were characterized by a PHI Quantera X-ray photoelectron spectroscope (XPS) with Al KR X-ray excitation source of 1.487 keV, with the 284.8 eV binding energy of the C 1s peak used for calibration. After being cycled to the desired state, the cells were disassembled inside the glovebox. The extracted cathodes were washed with dimethyl carbonate (DMC) three times and then dried under vacuum for further XPS measurement.

Electrochemical measurements

The Li_2MnO_3 cathode material (ball-milled or pristine), carbon black (Super P C65) and polyvinylidene fluoride (PVDF) were mixed in a 70:20:10 weight ratio in N-methyl-2-pyrrolidone (NMP) using a Thinky mixer. The slurry was coated on aluminum foil with a doctor blade and then dried in a vacuum oven at 80 °C overnight, resulting in a 2 mg active material loading per cathode (12.5 mm diameter). Coin cells were assembled using lithium foil, one piece of Celgard 2325, and 80 µL of 1 M $LiPF_6$ in 3:7 ethylene carbonate (EC): ethyl methyl carbonate (EMC) (LP57 from Gotion) as the counter electrode, separator, and electrolyte, respectively. Electrochemical experiments were measured on a LANHE battery test instrument at room temperature, with constant current charges set at a 10 mA/g current density with a voltage window

between 2.0 and 4.6 V vs Li^+/Li. The amount of ZrO_2 contaminant introduced by ball milling was calculated using the RIR method based on an XRD measurement. The current applied and gravimetric specific capacity reported were normalized to the weight of Li_2MnO_3 cathode material only.

DEMS measurements

Swagelok-type cells were assembled with the same cathode slurry composition (70:20:10) coated onto aluminum foil or stainless-steel mesh for DEMS outgassing measurements. The loading density was around 1 mg active material for aluminum foil cathodes and 10 mg for stainless-steel mesh cathodes. Cells were assembled with two separators, one polypropylene (Celgard 2500) and one glass fiber (Whatman), with the Celgard in direct contact with the cathode. Lithium metal foil was used as the anode. Off-gassing measurements were conducted using a custom-built differential electrochemical mass spectrometer as described by McCloskey et al.[18] To achieve quantifiable results, calibrations were performed for each gas of interest (O_2 and CO_2) to relate the ion current detected by the mass spectrometer to the partial pressure of the gas of interest in argon.

Mass spectrometer acid titrations

A similar setup as that used for DEMS measurements was used to monitor the gases evolved during an acid titration of cathodes extracted from cycled batteries.[19] During this titration, in which an extracted cathode (washed three times with DMC and vacuum dried) is placed in a vessel attached to the DEMS gas handling unit followed by

injection of 10 M H_2SO_4, carbonates on the cathode surface react with acid to produce CO_2 gas:

$$Li_2CO_3 + 2H^+ \rightarrow 2Li^+ + H_2O + CO_2 \quad (1)$$

In addition, peroxo-like species (O_2^{2-}) on the cathode react to form O_2 gas similarly to the reaction between lithium peroxide and acid:

$$Li_2O_2 + 2H^+ \rightarrow 2Li^+ + H_2O + \tfrac{1}{2} O_2 \quad (2)$$

Control experiments confirm that these surface species react to form stoichiometric amounts of gas as detected by the mass spectrometer.[20]

Warder titrations

In order to measure carbonate content more quickly than the above mass spectrometer method, a chemical titration was also employed. In this titration, DMC-rinsed and dried cathodes are sealed inside a septum-cap vial filled with argon. Nitrogen-sparged water is added to the sample. Five minutes are allowed for surface species present on the sample to dissolve in the water. Then phenolphthalein indicator is added, turning the solution bright pink due to the dissolved basic salts (pH ~11). The solution is titrated with dilute hydrochloric acid until it turns clear (pH = 8.2). Then mixed bromocresol green-methyl red indicator is added, turning the sample blue. The solution is titrated again until it turns pink (pH = 4.5). The entire process is conducted under air-free conditions.

In the first titration, lithium hydroxide is completely neutralized, and lithium carbonate is partially neutralized to lithium bicarbonate in solution:

$LiOH + H^+ \rightarrow H_2O + Li^+$ (3)

$Li_2CO_3 + H^+ \rightarrow LiHCO_3 + Li^+$ (4)

In the second titration, lithium bicarbonate is neutralized:

$LiHCO_3 + H^+ \rightarrow H_2CO_3 + Li^+$ (5)

Calibrations were performed on both Li_2CO_3 and LiOH to ensure quantifiable results.

Closed-cell pressure measurements

Pressure measurements were conducted using a similar setup to outgassing measurements. Instead of sweeping gas from the cell to a mass spectrometer, the cell was kept isolated, and the headspace pressure was monitored.

3. Results and discussions

3.1 Structure and surface contaminants

Figure 1a shows the XRD results of the pristine Li_2MnO_3 and its ball-milled counterparts. While the pristine Li_2MnO_3 is well-indexed by the Li_2MnO_3 PDF card (ICDD 04-11-3411), the BMP and BMC-F materials both have broadening diffraction peaks for the (001), (130), (131), $(\bar{1}33)$ and $(\bar{3}31)$ planes. By comparing Figures 1b and 1c,1d, it is not clear that the primary crystallite size of the two ball-milled samples has been significantly reduced after ball milling, so the broadening of the peaks is attributed to the strain induced by ball mill treatment. Notably, two additional peaks emerge at 30.4° and 31.7°, which can be indexed to ZrO_2 (ICDD 00-050-1089 and ICDD 04-012-0882), considering that ZrO_2 balls are used as the milling media. Reference Intensity

Ratio (RIR) quantitative method is employed to calculate the amount of the ZrO_2 impurity, based on the following equation:

$$I_{Li2MnO3} / I_{ZrO2} = (I_{c,\ Li2MnO3} / I_{c,\ ZrO2}) \bullet (X_{Li2MnO3} / X_{ZrO2}) \quad (6)$$

where I and Ic denote the experimental integral intensity and reference intensity ratio (α-Al_2O_3 as the reference) of certain diffraction peaks, respectively, and $X_{Li2MnO3} / X_{ZrO2}$ represents the weight ratio of the two compounds. In the case of a severely distorted (001) plane caused by strain, the data values from the (131) plane are applied to equation (6). The calculation is shown in the Supporting Information, Table S1 and the calculated weight percentage value of the ZrO_2 impurity is 4.5 wt.% and 5.6 wt.% for the BMP and BMC-F materials, respectively.

The results of the TEM experiments tell more information about the local structure of the two ball-milled materials. As shown in Figure 2a, the plane distance of (200), $(20\bar{1})$ and (110) are found to match the lattice of Li_2MnO_3 (C2/m), which confirms the bulk BMP material still possesses the Li_2MnO_3 structure. However, in Figures 2b-d, the results for the BMC-F sample show the bi-crystal frameworks. In the case of Figure 2c, the planes 0.25 nm and 0.22 nm can be assigned to the (040) and (130) planes of Li_2MnO_3, respectively. In Figure 2d, one can see an example of a $LiMnO_2$ ($R\bar{3}m$) particle where the indexed planes are {111} in both cases and have both a d-spacing of 0.25 nm. This suggests the possibility of generating a Li_2MnO_3 and $LiMnO_2$ composite phase after using a C-F additive during the ball mill treatment. This is reflected by the early stage sloped potential curve of the BMC-F material shown later. Furthermore, in Figure 2e, the carbon layer characteristic observed on the surface of the BMC-F sample

reminds us that new surface chemical species could be induced after ball mill treatment. Figures 2bi and 2bii reflect the overlap of the simulated reflection planes for each crystalline structure that matches the calculated zone axis. By selecting another zone axis pair, Figure Sxxx differentiates the Li2MnO3 and LiMnO2 phases with more detailed explanations.

A two-step Warder titration method is used with HCl as the titration reagent to quantify the surface carbonate species, which are inevitably present on oxide surfaces after synthesis and handling. Table 1 gives the quantitative results of the carbonate species for the three materials as-synthesized and after soaking the powder in the LP57 electrolyte. For pristine Li_2MnO_3, a 0.46 wt.% Li_2CO_3 is initially present, followed by a 0.57 wt.% carbonate species after electrolyte soaking, reasonably matching the results reported by Guerrini et al.[7] Interestingly, for the BMP material, 1.0 wt.% Li_2CO_3 is present in the as-synthesized material, which increases to 3.1 wt.% carbonate species upon exposure to the electrolyte. As for the BMC-F material, the Li_2CO_3 content is 14.0 wt.% as-synthesized and increases to 16.0 wt.% carbonate species after soaking in the electrolyte. As shown in Figure S1, certain minor peaks of the BMC-F XRD plot could also be indexed to the Li_2CO_3 phase (ICDD 04-010-5115). Overall, it is demonstrated that the BMP and, in particular, BMC-F materials contain large amounts of Li_2CO_3 contaminant, clearly indicating that new carbonate species will form once the ball-milled materials are exposed to the carbonate electrolyte. Furthermore, our ball-milling procedure also appears to increase carbonate content, presumably due to a combination of handling under ambient conditions and a reaction with the graphitic

fluoride (in the case of BMC-F). Our results highlight the need to understand and control the ball milling conditions to reduce the formation of unwanted carbonate species, which, as we will show later, have a large effect on outgassing. The following experiments were used to observe the oxidation state of the Mn ion, the gaseous products, and the pressure of the closed cell system. The issue of interfacial instability caused by ball milling is highlighted.

3.2 Pristine Li_2MnO_3 electrochemical performances

The electrochemical properties of pristine Li_2MnO_3 are evaluated by half-cell assembly vs Li^+/Li. Initial charge/discharge profiles are shown in Figure 3a, which reflect the initial cycle specific charge capacity of 31 mAh/g in the 2.0-4.6 V potential window at 10 mA/g current density. This capacity is consistent with Rana et al.[6] Figure 3b also shows the DEMS results, where CO_2 is the dominant gas product and O_2 gas is only faintly observed at the end of the first charge. Though the CO_2 onset is right at the starting point of the charging process, it continually grows and finally reaches 1.1 μmol g^{-1} min^{-1}. The amount of CO_2 is gradually diminished as the discharge process begins because the DEMS setup takes some time to sweep all of the gaseous product from the cell headspace to the mass spectrometer. The quantity of CO_2 attenuates slightly in the second cycle, which is also in agreement with Papp et al.[21]. For the pristine Li_2MnO_3, CO_2 is contributed from the decomposition of Li_2CO_3 or the carbonate electrolyte by a likely $2e^-/CO_2$ process, and O_2 is evolved from lattice oxygen oxidation by a $4e^-/O_2$ process.[20] As a result, Figure 3c plots the deconvolution of the total current of the CO_2 and O_2 and the sum of the current attributed to both gases. The green line represents the

total current contribution, while the gas evolution contributes a modest fraction of the total current, it is clear that another process is responsible for most of the current. Table 2 provides quantitative capacity contributions for the first cycle capacity for pristine Li_2MnO_3. There is a net 23.3 mAh/g capacity difference between the total capacity and the gas capacity, a value that matches Papp et al.[21], implying that this capacity is contributed by other redox processes. Figure 4 shows the Mn $2p_{3/2}$ XPS results for the pristine Li_2MnO_3 electrode at different cycles. The binding energy in the first charged state (CH1) is 642.3 eV, which shifts toward higher energy than 641.7 eV for the non-cycled state (0), indicating the oxidation of surface Mn from +3 to +4 during the first charge process.[22] Indeed, a residual Mn oxidation capacity is reported in Zhuo's work.[8] By combining those two results, we speculate that $Mn^{3+/4+}$ oxidation accounts for some of the remaining 23.3 mAh/g capacity in the first charge. While Zhuo et al. show that Mn reduction accounts for the whole first discharge capacity with surface Mn being at lower valence, with an average of +3.0, the first discharged state (DCH1) of Mn $2p_{3/2}$ spectrum in XPS does not show a lower energy shift compared the CH1, implying that the $Mn^{3+/4+}$ oxidation on charge is not reversible at the surface. It is quite interesting to see in Figure S2a that even second charged (CH2) and second discharged state (DCH2) show the presence of Mn^{4+}, but the fiftieth discharged state (DCH50) shows a return to lower $Mn^{3+/2+}$ oxidation states.

3.3 Purely ball-milled Li_2MnO_3 electrochemical performances

The BMP material has a substantial capacity increase compared to the pristine Li_2MnO_3, as its 210 mAh/g first charge specific capacity reported in Figure 5a clearly

shows. The DEMS data shown in Figure 5b also shows much different behavior from Figure 3b. Specifically, both O_2 and CO_2 gas can be detected near the beginning of the first charge process. The gas evolution rate increases with the charge potential, with a peak value of 0.6 and 1.7 μmol g^{-1} min^{-1} for O_2 and CO_2 gas, respectively. The second cycle also shows attenuated gas evolution with peak values of 0.2 μmol g^{-1} min^{-1} O_2 evolution and 1.2 μmol g^{-1} min^{-1} CO_2 evolution at the end of the second charge. Figure 5c simultaneously plots the voltage curve and current deconvolution curves for the BMP material. By the top of charge, gas evolution contributes almost all of the measured current. The total amount of O_2 ($4e^-$ process) and CO_2 ($2e^-$ process) capacity, listed in Table 2, are 30.2 and 47.1 mAh/g, respectively, along with 196.9 mAh/g total capacity recorded during the DEMS test, resulting in 119.6 mAh/g of capacity related to non-gas evolving processes. Since the theoretical capacity from Li_2CO_3 decomposition into CO_2 is 22.5 mAh/g, based on a $2e^-/CO_2$ process described in the pristine Li_2MnO_3 part, other reactions must be contributing to the additional CO_2 and O_2 evolution. The recent works by Rana et al. and Zhuo et al. have ruled out the possibility of $Mn^{4+/7+}$ oxidation as proposed by Radin et al.,[6, 8, 23] and according to the phase diagram depicted in Thackeray's work, when Li_2MnO_3 is charged above 4.4 V, "Li_2O" species is leached out, and the bulk material becomes MnO_2.[24] The oxidized oxygen ion can either evolve into O_2 gas or react with the electrolyte to possibly produce CO_2, suggesting the decomposition of the EC molecule accounting for the additional CO_2 for the BMP.[25] That leads us to question whether the charge capacity not related to gas evolution could be Mn ion oxidation. Since this work does not include

soft XAS TFY mode characterization on Mn, the Mn ion oxidation assumption cannot be proved here. Still, the large amount of excess capacity remains an interesting open question.

The Mn $2p_{3/2}$ XPS spectra show a 642.3 eV binding energy (B.E.) for both 0 and CH1 states with a signal to noise ratio (S/N) that allows us to confirm the presence of Mn at the material surface. The DCH1 state has an abysmal S/N ratio, making it impossible to detect Mn ions, implying that the surface is coated with a non-Mn containing solid layer, which we hypothesize are alkyl carbonates deposited due to electrolyte degradation. To quantify the change in carbonates on the material surface during cycling, CH1 and DCH1 electrodes are extracted from the coin cells and immersed in 10 M sulfuric acid in a hermetically sealed vessel, which leads to CO_2 gas production that is then used to quantify the amount of the carbonate species within the electrode. From the summarized results in Table 3, the carbonate species content in a BMP electrode charged to 4.6 V is 2.7 wt.% based on the weight of the BMP active material, which is slightly reduced compared to 3.1 wt.% for the electrolyte exposed BMP powder (Table 1), suggesting partial Li_2CO_3 decomposition during the charging process. The DCH1 state shows a notable increase of the carbonate species content to 13.0 wt.%, thereby explaining the poor S/N ratio of DCH1 – the surface of the electrode is covered by a thick layer of carbonates that were deposited after the first discharge. Interestingly, in Figure 6b O 1s XPS spectra, the area ratio between metal carbonate/C=O (~530.7 eV) and organic C-O (~532.2 eV) bonds of DCH1 increases against that of CH1 (from 1.5 to 2.1), which also supports the addition of carbonate

species after the discharge process. In an attempt to understand the origin of this deposition, we revisit an interesting observation from Papp et al., which reported the consumption during discharge of gases evolved during charge.[21] The same experimental setup is used here, in which the volume-calibrated cell headspace is isolated with an in-line pressure transducer, and Figure 7 presents the headspace pressure during the first cycle. This mode of operation mimics that of more conventional, closed system battery cells, such as the coin cells used to prepare the XPS samples. Based on Table 3, the total gas evolved by the end of the first charge was 2245 μmol/g, and gas evolution continues through most of the first discharge. Noticeably, the accumulated gas quantity starts to drop once the potential drops below 2.75 V with a highest 2577 μmol/g value, and in total, 401 μmol/g gas is consumed between 2.75 and 2.0 V. This observation successfully reproduces the finding by Papp et al. The gas consumption can likely be attributed to the reduction of O_2 gas to peroxide, further reacting with carbonate solvent and Li^+ to form lithium alkyl carbonate species, which are deposited on the surface of the cathode. From Figure S2b, the Mn XPS S/N ratio of sample CH2 (an XPS spectra of a BMP electrode at the top of a second 4.6 V charge) is improved, then becomes poor again in DCH2 (the second discharge to 2.0 V), indicating that the process of surface Li_2O leaching and carbonate species deposition through low potential discharge repeatedly occurs. Upon DCH50, the S/N becomes very strong, and the binding energy (B.E.) is 641.7 eV, suggesting that lower valence Mn is exposed to the surface after long term cycling, which behaves more effectively with Li_2O leaching. As reflected by Figure S3b, the specific capacity after 50 cycles has

decayed significantly to only 40 mAh/g.

3.4 C-F additive ball-milled Li_2MnO_3 electrochemical performances:

This section describes the behavior of the BMC-F material. Figure 8a shows that the material delivers a 320 mAh/g first charge specific capacity, comparable to the thoroughly studied Li-Mn rich NMC material.[26-27] In the Li-Mn rich NMC cathode, the low potential (< 4.4 V) region is usually assigned to transition metal oxidation such as $Co^{3+/4+}$ and $Ni^{2+/3+}$, followed by the characteristic 4.45 V plateau attributed to reversible oxygen redox reaction as shown by mRIXS.[28-29] Li-Mn rich NMC is a $Li_2MnO_3/LiMnO_2$ composite material, the same two phases identified in the BMC-F material.[26] The phase diagram in Thackery's work again shows the expected phase changes during de-lithiation, based on which the low potential sloped curve in Figure 8a is thought to represent $Mn^{3+/4+}$ oxidation.[24] In Figure 8b, no O_2 gas can be observed. In contrast, CO_2 gas emerges at the beginning of the first charge, rising linearly with the potential and reaching a maximum value of 3.6 μmol g^{-1} min^{-1} during the later stage of the ~4.4 V plateau. Once the voltage passes the plateau, the CO_2 amount quickly decreases to 2.9 μmol g^{-1} min^{-1} at 4.46 V and 2.2 μmol g^{-1} min^{-1} at 4.60 V, with an evident two-stage decay. In the second charge process, the CO_2 attenuates but still has the most significant peak value of 1.4 μmol g^{-1} min^{-1} among the three materials. Once more, as shown in Figure 8c, the difference between the total current and gas current decreases as the charging potential rises. At the 4.43 V plateau, the gas current appears to slightly exceed the theoretical current, dropping below the theoretical value at the end of the plateau. That could suggest a corrosive process, possibly related to CO_2 gas

generation from the decomposition of EC.[20] According to Table 2, the total amount of CO_2 capacity is 218.9 mAh/g, almost twice the 116.1 mAh/g expected if all of the Li_2CO_3 initially present in the material oxidized via a 2 e^-/Li_2CO_3 process. This suggests the decomposition of EC contributes substantially to the CO_2 capacity. CO_2 evolution contributes 218.9 mAh/g of the 329.8 mAh/g total capacity, indicating that 109.3 mAh/g results from other redox process, potentially including Mn oxidation from +3 to +4 state with $LiMnO_2$ in the non-cycled state.

While the S/N ratio of Mn $2p_{3/2}$ XPS spectra allows identification of Mn on the BMC-F surface for the 0, CH1 and DCH1 states, it is not strong enough to determine whether the surface Mn has a +3 oxidation state for the non-cycled electrode. However, the CH1 state has a B.E. at 642.3 eV, and the DCH1 state has a lower shifted B.E. at 641.7 eV, showing that surface Mn ions plausibly have a +4 state at the top of the first charge and are reduced back to a +3 state at the end of the first discharge. Based on Table 4, when the cell is charged to 4.0 V in the first cycle (roughly at the gas onset), the titration experiment gives a 17.0 wt.% carbonate species with a slight increase compared to the 16.0 wt.%, observed in the BMC-F electrolyte-soaked powder. This is evidence that Mn^{3+} oxidation to Mn^{4+} with no electrolyte decomposition mainly contributes to the capacity in the early stage of the first charge process. At the end of the first charge, 4.6 V, the carbonate species content is reduced to 5.6 wt.%, as is expected given the large amount of CO_2 evolved. The increase of the carbonate species to 12.0 wt.% at the end of discharge also implies the possible reduction of CO_2 gas during the discharge process, or the formation of electrolyte degradation products on

the electrode surface, presumably from electrolyte fragments that formed during charge. Similar to the BMP material, the O 1s spectra in Figure 9b of BMC-F material again shows that the ratio between metal carbonate/C=O (~530.7 eV) and organic C-O (~532.2 eV) is larger for DCH1 compared to that of CH1 (from 0.4 to 1.1). In Figure 10, where pressure rise is again monitored in an isolated cell headspace, it is found that the CO_2 evolution (the only gas that was found to evolve via DEMS in Fig. 8) still slightly continues during discharge, after a total of 1364 μmol/g CO_2 evolved during charge to 4.6 V. The CO_2 quantity decreases below 3.22 V, where a 1535 μmol/g maximum value is recorded, and 153 μmol/g CO_2 is consumed by the end of discharge, suggesting that CO_2 is reduced to carbonate species that deposit on the cathode's surface, analogous to the BMP material. From Figure S2c, the 642.3 eV B.E. and 641.7 eV B.E. suggest the oxidation and reduction of surface Mn ion are involved during the second charge and second discharge process, respectively. The S/N ratio of CH2 is also more substantial than DCH1 and DCH2, inferring that the cycle of Li_2CO_3 decomposition and CO_2 reduction repeats through the second cycle. Like the BMP XPS spectra, the DCH50 Mn $2p_{3/2}$ spectrum in BMC-F material has a solid S/N ratio and an even smaller B.E. than 641.7 eV, indicating lower valence $Mn^{3+/2+}$ is exposed to the surface of the BMC-F material after long term cycling process. Due to the irreversibility of Li_2CO_3/electrolyte decomposition, and even Mn migration in the bulk structure, the specific capacity degrades gradually and only preserves 50 mAh/g at DCH50 in Figure S3c.[4, 30]

4. Conclusions

This paper introduces ball milling to activate the high-temperature solid-state synthesized Li_2MnO_3 cathode material. We identify the Li_2MnO_3 phase for BMP material and Li_2MnO_3/$LiMnO_2$ composite phases for BMC-F material by combining XRD and TEM techniques. Through acid titration, DEMS and XPS characterizations, within the 2.0-4.6 V vs Li^+/Li potential window, pristine Li_2MnO_3 is found to have less residual amount of Li_2CO_3 and a 31 mAh/g first charge specific capacity. While a 210 mAh/g and 320 mAh/g first charge capacity are delivered by the BMP and BMC-F material, respectively, it is found that large amounts of Li_2CO_3 existed, which is further electrochemically active releasing CO_2 during the cycling process. However, due to the highly irreversible nature of the Li_2CO_3/electrolyte decomposition, the first discharge capacity of the BMP and BMC-F materials is only 155 and 170 mAh/g, respectively. Such surface instability degrades the surface of the crystal and leads to continuously capacity fade during cycling. Although the electrochemical capacity is significantly increased, the surface effects caused by ball milling should be studied further in order to determine whether this method can be applied to activate Mn-containing novel cathode materials.[31]

Acknowledgement

This work was supported by the Assistant Secretary for Energy Efficiency and Renewable Energy, Vehicle Technologies Office, under the Applied Battery Materials Program, of the U.S. Department of Energy (DOE) under contract no. DE-AC05-00OR22725.

Corresponding Author

Atin Pramanik (atinpramanik1990@gmail.com), Bryan D. McCloskey (bmcclosk@berkeley.edu), Pulickel M. Ajayan (ajayan@rice.edu)

Conflict of interest

There are no known conflicts to declare.

ORCID

Lori Kaufman 0000-0001-5815-4123

Francisco C. Robles Hernández 0000-0001-5587-0802

Atin Pramanik 0000-0002-3954-7770

Ganguli Babu 0000-0002-8609-4890

Nanda Jagjit 0000-0002-6875-0057

Bryan D. McCloskey 0000-0001-6599-2336

Pulickel M. Ajayan 0000-0001-8323-7860

References

1. Nitta, N.; Wu, F.; Lee, J. T.; Yushin, G., Li-ion battery materials: present and future. *Mater. Today* **2015,** *18*, 252-264.
2. Liu, W.; Oh, P.; Liu, X.; Lee, M.-J.; Cho, W.; Chae, S.; Kim, Y.; Cho, J., Nickel-rich layered lithium transition-metal oxide for high-energy lithium-ion batteries. *Angew. Chem. Int. Ed.* **2015,** *54*, 4440-4457.
3. Armstrong, A. R.; Dupre, N.; Paterson, A. J.; Grey, C. P.; Bruce, P. G., Combined Neutron Diffraction, NMR, and for layer to spinel transformation of $LiMnO_2$. *Chem. Mater.* **2004,** *16*, 3106-3118.
4. Zhan, C.; Wu, T.; Lu, J.; Amine, K., Dissolution, migration, and deposition of transition metal ions in Li-ion batteries exemplified by Mn-based cathodes – a critical review. *Energy Environ. Sci.* **2018,** *11*, 243-257.
5. Yu, D. Y. W.; Yanagida, K.; Kato, Y.; Nakamura, H., Electrochemical Activities in Li_2MnO_3. *J. Electrochem. Soc.* **2009,** *156*, A417-A424.
6. Rana, J.; Papp, J. K.; Lebens-Higgins, Z.; Zuba, M.; Kaufman, L. A.; Goel, A.; Schmuch, R.; Winter,

M.; Whittingham, M. S.; Yang, W.; McCloskey, B. D.; Piper, L. F. J., Quantifying the Capacity Contributions during Activation of Li_2MnO_3. *ACS Energy Lett.* **2020,** *5*, 634-641.

7. Guerrini, N.; Jin, L.; Lozano, J. G.; Luo, K.; Sobkowiak, A.; Tsuruta, K.; Massel, F.; Duda, L.-C.; Roberts, M. R.; Bruce, P. G., Charging Mechanism of Li_2MnO_3. *Chem. Mater.* **2020,** *32*, 3733-3740.

8. Zhuo, Z.; Dai, K.; Qiao, R.; Wang, R.; Wu, J.; Liu, Y.; Peng, J.; Chen, L.; Chuang, Y.-d.; Pan, F.; Shen, Z.-x.; Liu, G.; Li, H.; Devereaux, T. P.; Yang, W., Cycling mechanism of Li_2MnO_3: Li–CO_2 batteries and commonality on oxygen redox in cathode materials. *Joule* **2021,** *5*, 975-997.

9. Clément, R. J.; Lun, Z.; Ceder, G., Cation-disordered rocksalt transition metal oxides and oxyfluorides for high energy lithium-ion cathodes. *Energy & Environ. Sci.* **2020,** *13*, 345-373.

10. Chen, D.; Ahn, J.; Chen, G., An Overview of Cation-Disordered Lithium-Excess Rocksalt Cathodes. *ACS Energy Lett.* **2021,** *6*, 1358-1376.

11. Li, L.; Ahn, J.; Yue, Y.; Tong, W.; Chen, G.; Wang, C., Fluorination-Enhanced Surface Stability of Disordered Rocksalt Cathodes. *Adv. Mater.* **2022,** *34*, 2106256.

12. Yabuuchia, N.; Takeuchib, M.; Nakayamac, M.; Shiibac, H.; Ogawae, M.; Nakayamae, K.; Ohtae, T.; Endof, D.; Ozakif, T.; Inamasuf, T.; Satoa, K.; Komabab, S., High-capacity electrode materials for rechargeable lithium batteries Li_3NbO_4 -based system with cation-disordered rocksalt structure. *PNAS* **2015,** *112*, 7650-7655.

13. Kan, W. H.; Chen, D.; Papp, J. K.; Shukla, A. K.; Huq, A.; Brown, C. M.; McCloskey, B. D.; Chen, G., Unravelling Solid-State Redox Chemistry in $Li_{1.3}Nb_{0.3}Mn_{0.4}O_2$ Single-Crystal Cathode Material. *Chem. Mater.* **2018,** *30*, 1655-1666.

14. Chen, D.; Kan, W. H.; Chen, G., Understanding Performance Degradation in Cation-Disordered Rock-Salt Oxide Cathodes. *Adv. Energy Mater.* **2019,** *9* (31), 1901255.

15. Huang, B.; Wang, R.; Gong, Y.; He, B.; Wang, H., Enhanced Cycling Stability of Cation Disordered Rock-Salt $Li_{1.2}Ti_{0.4}Mn_{0.4}O_2$ Material by Surface Modification With Al_2O_3. *Front. Chem.* **2019,** *7*, 107.

16. Kataoka, R.; Kojima, T.; Takeichi, N., Electrochemical Property of Li-Mn Cation Disordered Li-Rich Li_2MnO_3 with NaCl Type Structure. *J. Electrochem. Soc.* **2018,** *165* (2), A291-A296.

17. Yan, P.; Xiao, L.; Zheng, J.; Zhou, Y.; He, Y.; Zu, X.; Mao, S. X.; Xiao, J.; Gao, F.; Zhang, J.-G.; Wang, C.-M., Probing the Degradation Mechanism of Li_2MnO_3 Cathode for Li-Ion Batteries. *Chem. Mater.* **2015,** *27*, 975-982.

18. McCloskey, B. D.; Bethune, D. S.; Shelby, R. M.; Girishkumar, G.; Luntz, A. C., Solvents' Critical Role in Nonaqueous Lithium-Oxygen Battery Electrochemistry. *J. Phys. Chem. Lett.* **2011,** *2*, 1161-1166.

19. Renfrew, S. E.; McCloskey, B. D., Quantification of Surface Oxygen Depletion and Solid Carbonate Evolution on the First Cycle of $LiNi_{0.6}Mn_{0.2}Co_{0.2}O_2$ Electrodes. *ACS Appl. Energy Mater.* **2019,** *2*, 3762-3772.

20. Renfrew, S. E.; McCloskey, B. D., Residual Lithium Carbonate Predominantly Accounts for First Cycle CO_2 and CO Outgassing of Li-Stoichiometric and Li-Rich Layered Transition-Metal Oxides. *J. Am. Chem. Soc.* **2017,** *139*, 17853-17860.

21. Papp, J. K.; Li, N.; Kaufman, L. A.; Naylor, A. J.; Younesi, R.; Tong, W.; McCloskey, B. D., A comparison of high voltage outgassing of $LiCoO_2$, $LiNiO_2$, and Li_2MnO_3 layered Li-ion cathode materials. *Electrochim. Acta* **2021,** *368*, 137505.

22. Quesne-Turin, A.; Flahaut, D.; Croguennec, L.; Vallverdu, G.; Allouche, J.; Charles-Blin, Y.; Chotard, J. N.; Menetrier, M.; Baraille, I., Surface Reactivity of Li_2MnO_3: First-Principles and

Experimental Study. *ACS Appl. Mater. Interfaces* **2017,** *9*, 44222-44230.
23. Radin, M. D.; Vinckeviciute, J.; Seshadri, R.; Van der Ven, A., Manganese oxidation as the origin of the anomalous capacity of Mn-containing Li-excess cathode materials. *Nat. Energy* **2019,** *4*, 639-646.
24. Thackeray, M. M.; Johnson, C. S.; Vaughey, J. T.; Li, N.; Hackney, S. A., Advances in manganese-oxide 'composite' electrodes for lithium-ion batteries. *J. Mater. Chem.* **2005,** *15*, 2257-2267.
25. Freiberg, A. T. S.; Roos, M. K.; Wandt, J.; de Vivie-Riedle, R.; Gasteiger, H. A., Singlet Oxygen Reactivity with Carbonate Solvents Used for Li-Ion Battery Electrolytes. *J. Phys. Chem. A* **2018,** *122*, 8828-8839.
26. Thackeray, M. M.; Kang, S.-H.; Johnson, C. S.; Vaughey, J. T.; Benedek, R.; Hackney, S. A., Li_2MnO_3-stabilized $LiMO_2$ (M = Mn, Ni, Co) electrodes for lithium-ion batteries. *J. Mater. Chem.* **2007,** *17*, 3112-3125.
27. Nayak, P. K.; Grinblat, J.; Levi, M.; Levi, E.; Kim, S.; Choi, J. W.; Aurbach, D., Al Doping for Mitigating the Capacity Fading and Voltage Decay of Layered Li and Mn-Rich Cathodes for Li-Ion Batteries. *Adv. Energy Mater.* **2016,** *6*, 1502398.
28. Hu, E.; Yu, X.; Lin, R.; Bi, X.; Lu, J.; Bak, S.; Nam, K.-W.; Xin, H. L.; Jaye, C.; Fischer, D. A.; Amine, K.; Yang, X.-Q., Evolution of redox couples in Li- and Mn-rich cathode materials and mitigation of voltage fade by reducing oxygen release. *Nat. Energy* **2018,** *3*, 690-698.
29. Yang, W.; Devereaux, T. P., Anionic and cationic redox and interfaces in batteries: Advances from soft X-ray absorption spectroscopy to resonant inelastic scattering. *J. Power Sources* **2018,** *389*, 188-197.
30. Amalraj, S. F.; Burlaka, L.; Julien, C. M.; Mauger, A.; Kovacheva, D.; Talianker, M.; Markovsky, B.; Aurbach, D., Phase Transitions in Li_2MnO_3 Electrodes at Various States-of-Charge. *Electrochim. Acta* **2014,** *123*, 395-404.
31. Ahn, J.; Chen, D.; Chen, G., A Fluorination Method for Improving Cation-Disordered Rocksalt Cathode Performance. *Adv. Energy Mater.* **2020,** *10*, 2001671.

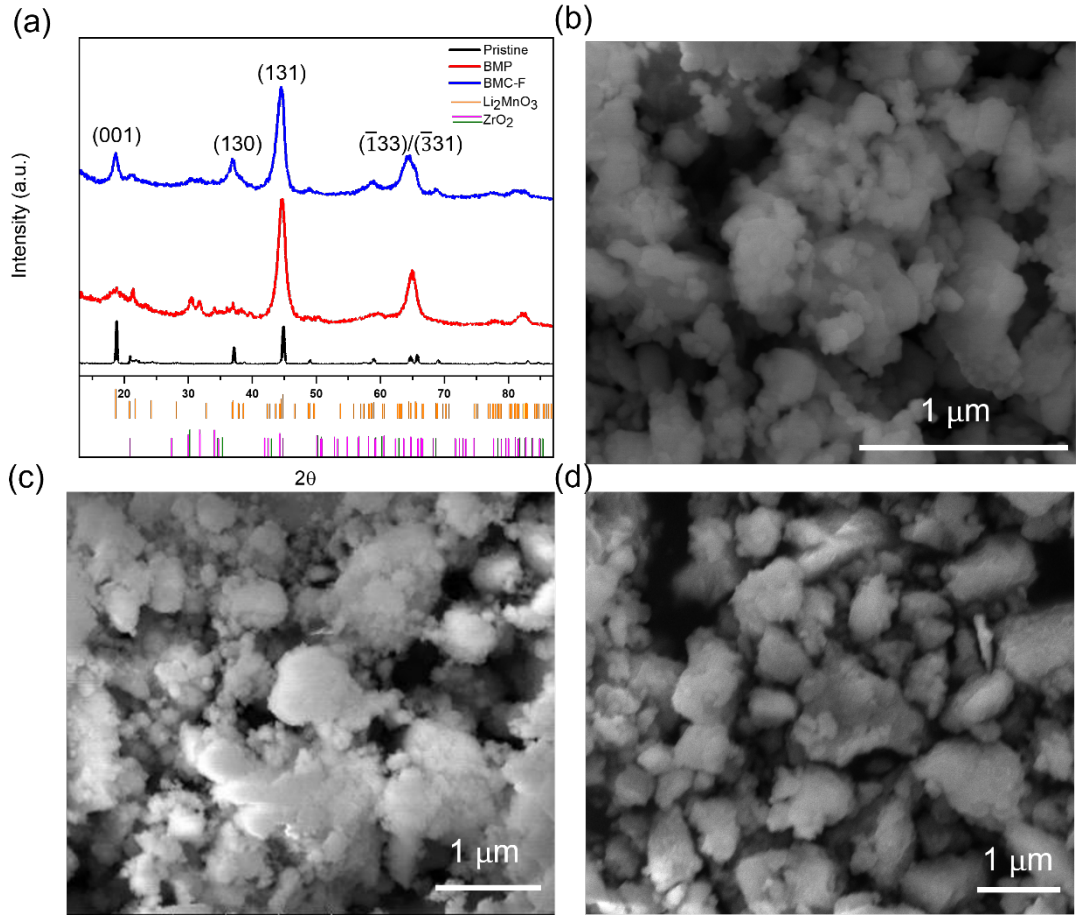

Figure 1. (a) XRD results of pristine Li_2MnO_3, BMP and BMC-F materials; SEM images of pristine Li_2MnO_3 (b), BMP (c) and BMC-F materials (d).

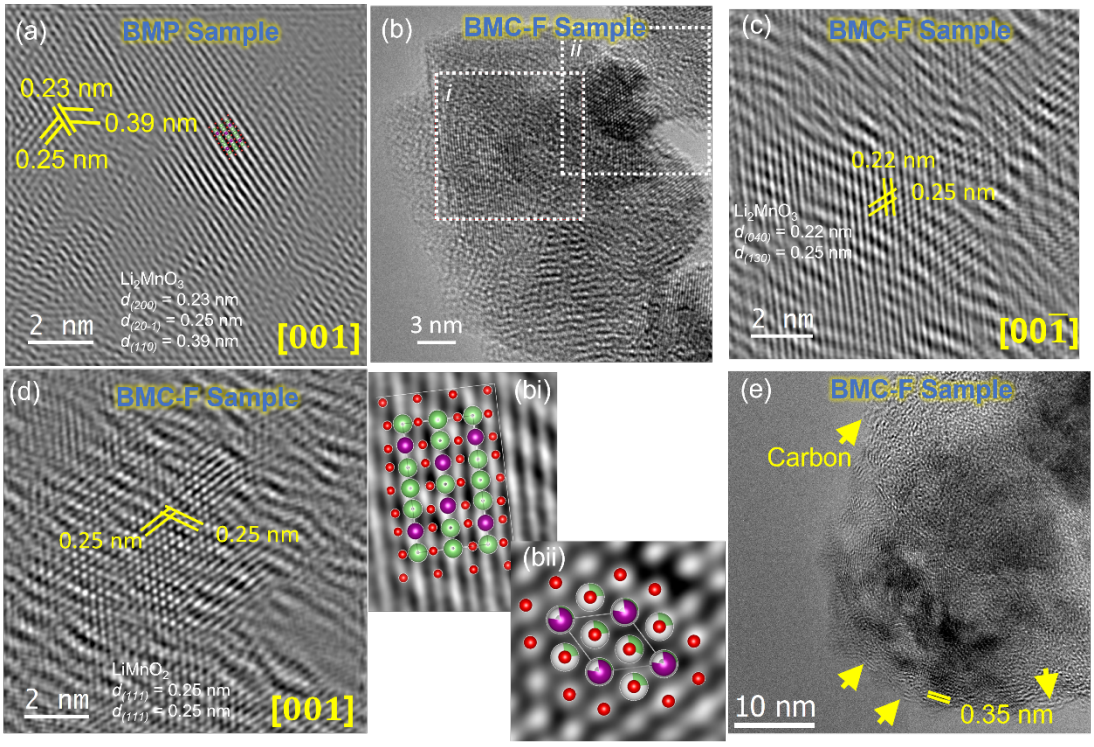

Figure 2. (a) TEM results of BMP sample, where lattice spacing of Li_2MnO_3 phase is indexed; (b) TEM results of BMC-F sample, (bi) Li_2MnO_3 structure simulation, (bii) $LiMnO_2$ structure simulation (red O atom, green Li atom and purple Mn atom); (c) and (d) index of lattice spacing of Li_2MnO_3 and $LiMnO_2$ phase for the BMC-F sample, respectively; (e) Surface of the BMC-F sample is covered by 2-3 nm graphitic carbon.

Table 1. Quantification of the carbonate species by the two-step Warder titration using HCl.

Carbonate content (wt.%)	Pristine	BMP	BMC-F
Powder as synthesized	0.46 %	1.0 %	14.0 %
Powder electrolyte exposed	0.57 %	3.1 %	16.0 %

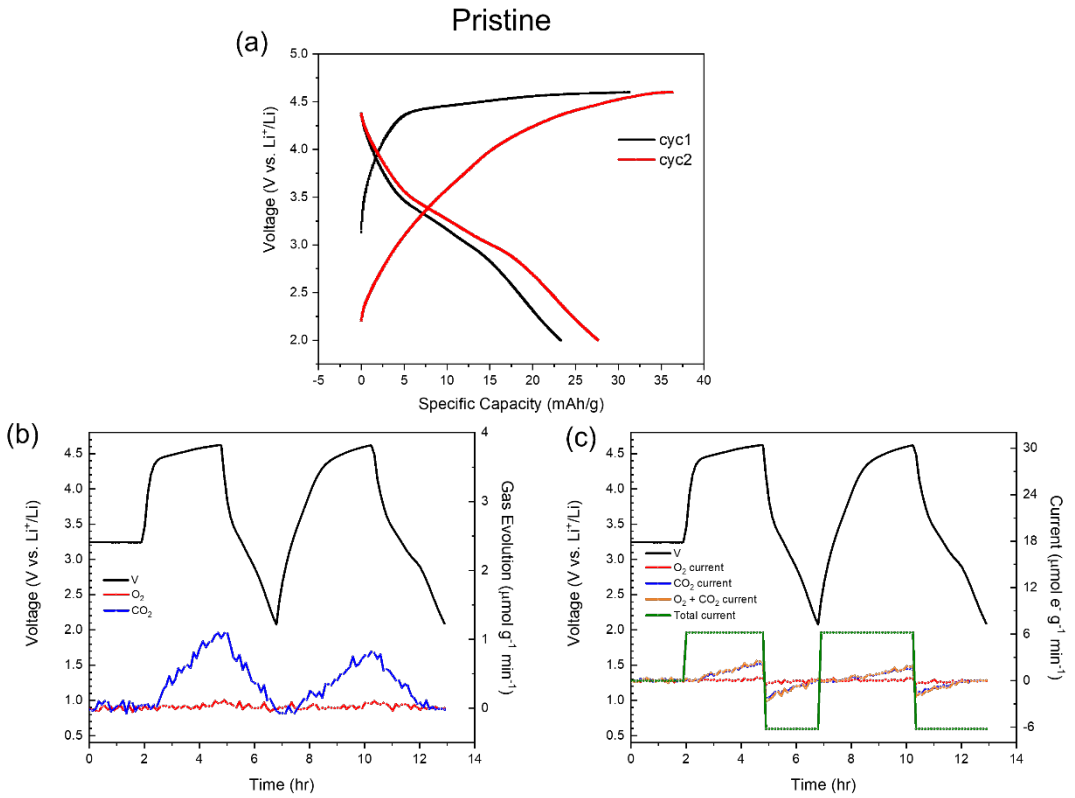

Figure 3. (a) First two cycles electrochemical capacity of pristine Li_2MnO_3; (b) Gas evolution from pristine Li_2MnO_3 for the first two cycles; (c) Capacity deconvolution of (b). (The test condition is a 10 mA/g current density based on the Li_2MnO_3 cathode material, with a 2.0-4.6 V vs. Li^+/Li potential window.)

Table 2. Quantification of the first charge capacity contributions for Pristine, BMP and BMC-F from DEMS tests. O_2 and CO_2 capacities are calculated through data presented in Fig. 3c, assuming a 4 e^-/O_2 and 2 e^-/CO_2 process, respectively, while the total electrochemical capacity during the first charge is provided in the 'Total' column, and the difference between the electrochemical capacity and gas capacity is listed in the 'Total – gas' column.

Materials	O_2 (mAh/g)	CO_2 (mAh/g)	Total (mAh/g)	Total - Gas (mAh/g)
Pristine	0.5	5.1	28.9	23.3
BMP	30.2	47.1	196.9	119.6
BMC-F	1.6	218.9	329.8	109.3

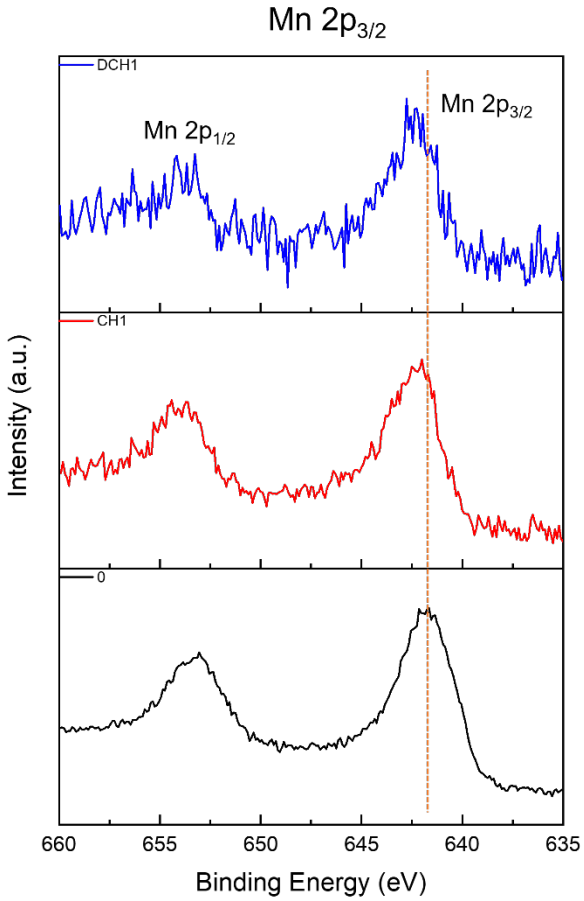

Figure 4. Mn $2p_{3/2}$ XPS spectra of pristine Li_2MnO_3 electrodes for non-cycled state (0), first charged 4.6 V state (CH1) and first discharged 2.0 V state (DCH1).

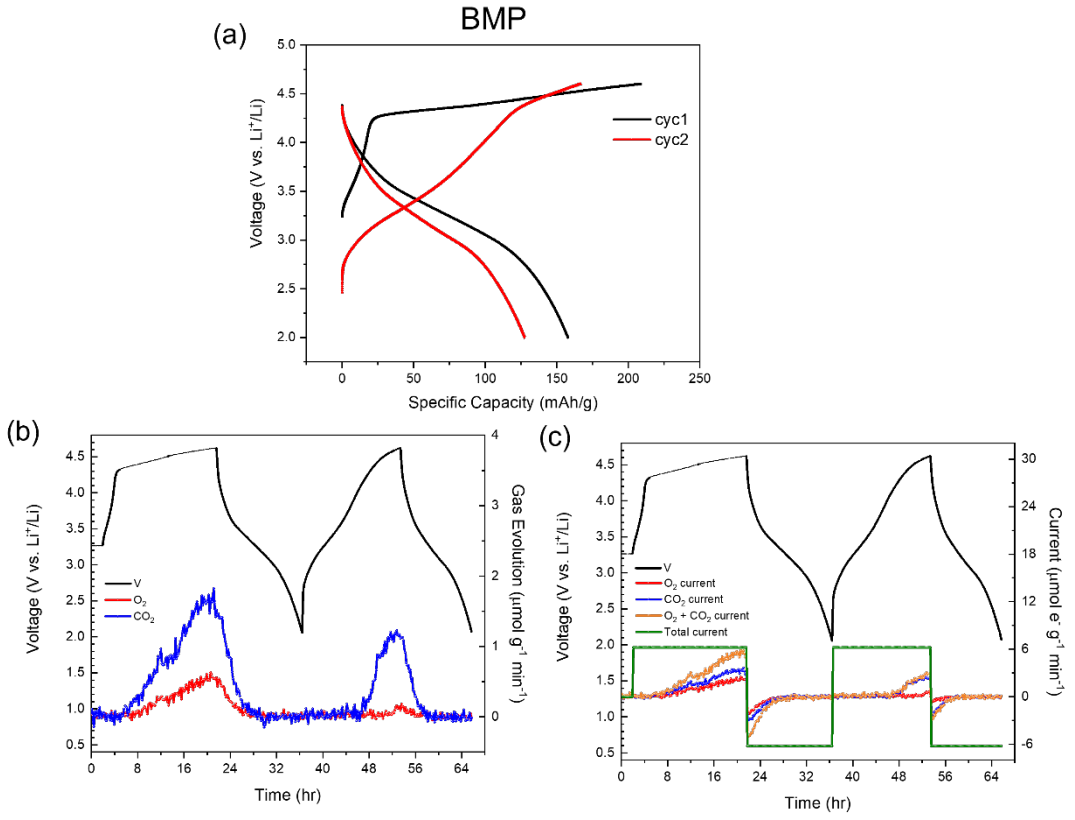

Figure 5. (a) First two cycles electrochemical capacity of BMP; (b) Gas evolution from BMP for the first two cycles; (c) Capacity deconvolution of (b). (The test condition is a 10 mA/g current density based on the Li_2MnO_3 cathode material, with a 2.0-4.6 V vs. Li^+/Li potential window.)

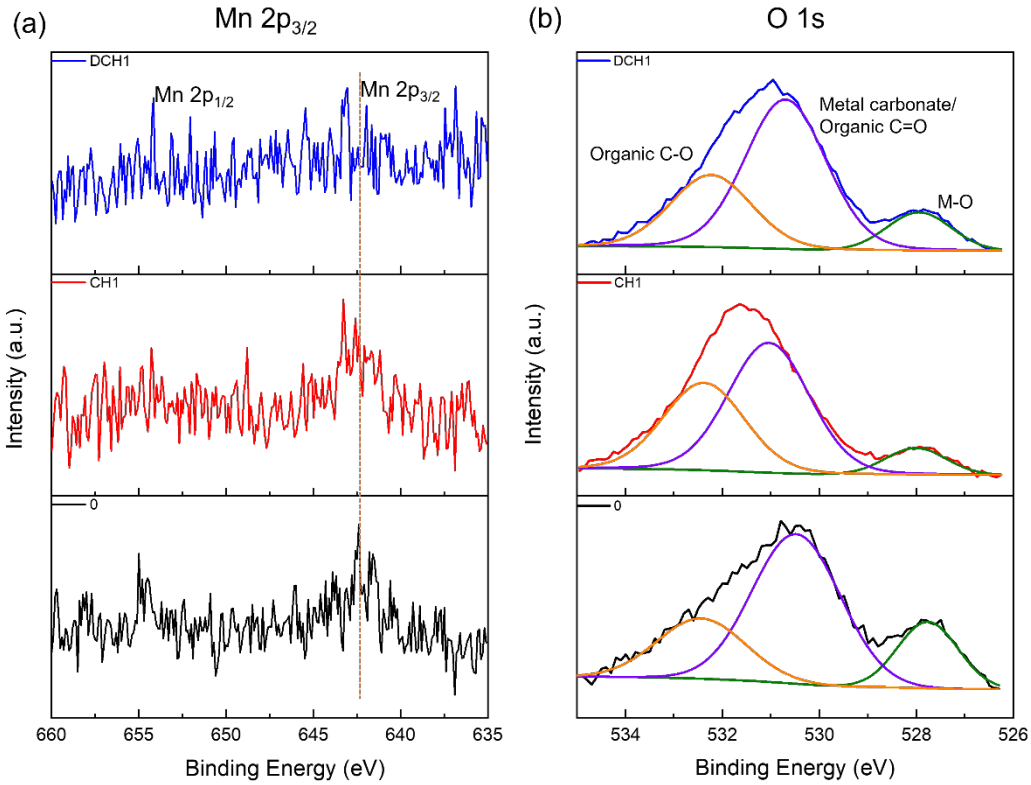

Figure 6. Mn $2p_{3/2}$ (a) and O 1s (b) XPS spectra of BMP electrodes for non-cycled state (0), first charged 4.6 V state (CH1) and first discharged 2.0 V state (DCH1).

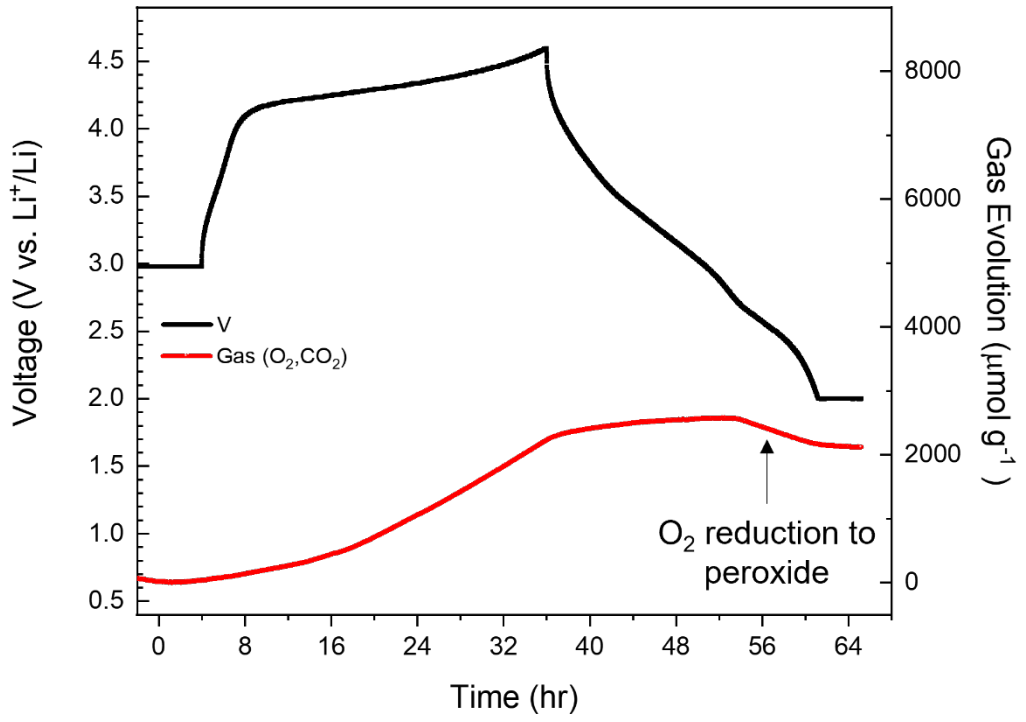

Figure 7. Closed-cell pressure test of the BMP material for the first cycle. Instead of sweeping gas from the cell to a mass spectrometer, the cell was kept isolated, and the headspace pressure was monitored.

Table 3. Quantification of carbonate species, accumulated, and consumed gases during cycling of BMP material.

BMP State	Carbonate content (wt.%)	Gas accumulation (µmol/g)	Gas consumption (µmol/g) against highest recorded value
CH1 4.6 V	2.7 %	2245	NA
DCH1 2.75 V	NA	2577	0
DCH1 2.0 V	13.0 %	2176	401
DCH1 2.0 V (Hold)	NA	2114	463

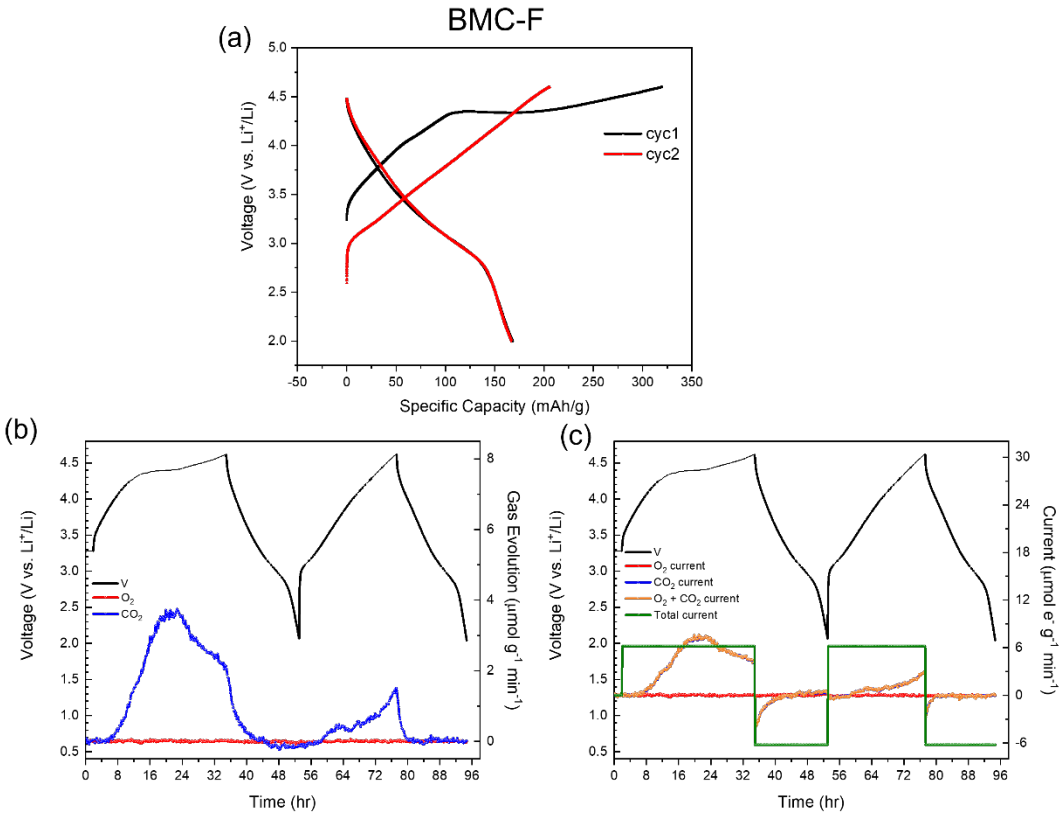

Figure 8. (a) First two cycles electrochemical capacity of BMC-F; (b) Gas evolution from BMC-F for the first two cycles; (c) Capacity deconvolution of (b). (The test condition is a 10 mA/g current density based on the $Li_2MnO_3/LiMnO_2$ cathode material, with a 2.0-4.6 V vs. Li^+/Li potential window.)

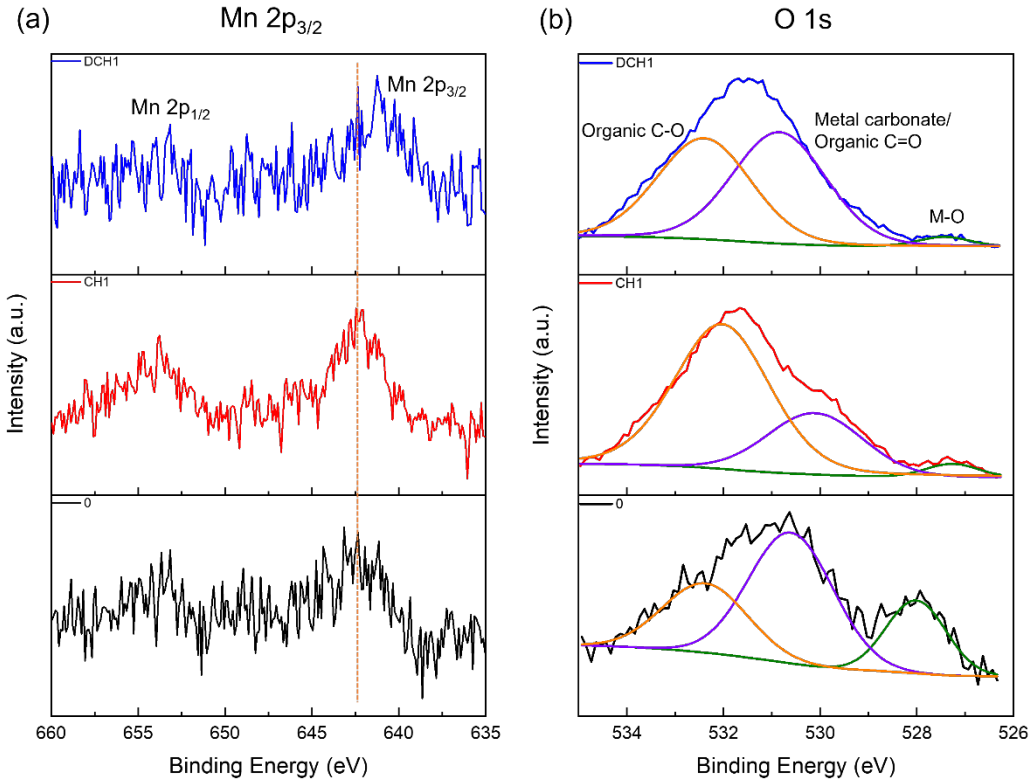

Figure 9. Mn $2p_{3/2}$ (a) and O 1s (b) XPS spectra of BMC-F electrodes for non-cycled state (0), first charged 4.6 V state (CH1) and first discharged 2.0 V state (DCH1).

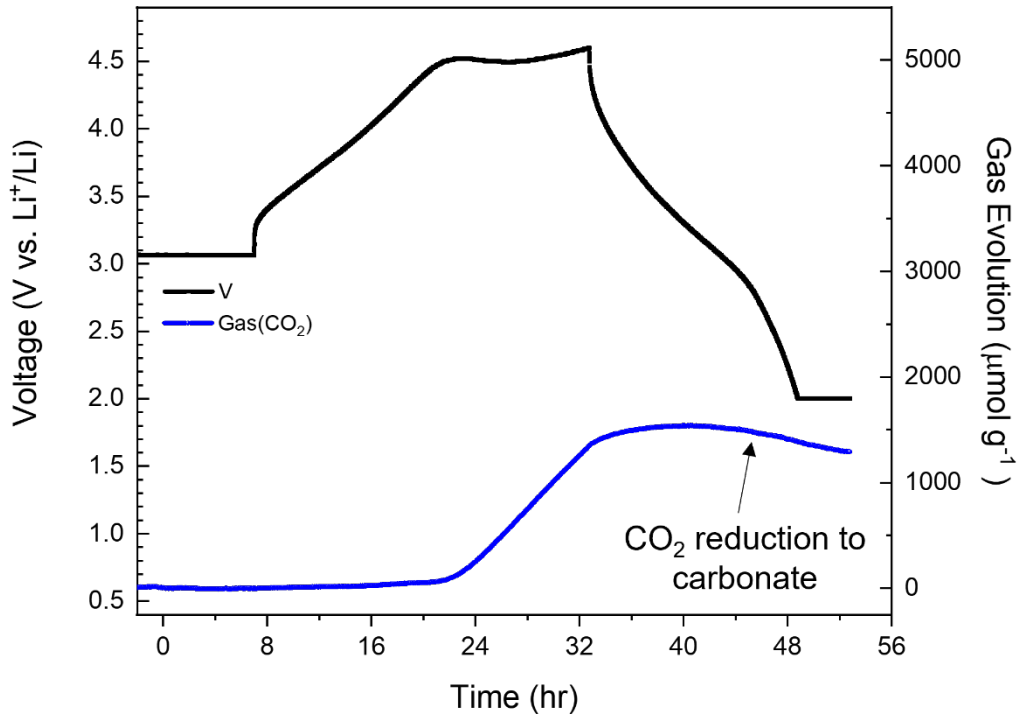

Figure 10. Closed cell pressure test of BMC-F material for the first cycle. Instead of sweeping gas from the cell to a mass spectrometer, the cell was kept isolated, and the headspace pressure was monitored.

Table 4. Quantification of carbonate species, accumulated, and consumed gases during cycling of BMC-F material.

BMC-F State	Carbonate content (wt.%)	Gas accumulation (µmol/g)	Gas consumption (µmol/g) against highest recorded value
CH1 4.0 V	17.0 %	25	NA
CH1 4.6 V	5.6 %	1364	NA
DCH1 3.22 V	NA	1535	0
DCH1 2.0 V	12.0 %	1382	153
DCH1 2.0 V (Hold)	NA	1303	232